

Electromagnetic Design Characterization of Synchronous Machines with Flux Switching Effect Employing Reluctance Rotors and Stators with PMs and AC Concentrated Coils

Oluwaseun A. Badewa, *Student Member, IEEE*, Ali Mohammadi, *Student Member, IEEE*,
Donovin D. Lewis, *Student Member, IEEE*, Somasundaram Essakiappan*, *Senior Member, IEEE*,
Madhav Manjrekar*, *Senior Member, IEEE*, and Dan M. Ionel, *Fellow, IEEE*.

Abstract—This paper introduces an innovative design for a synchronous electric motor that has phase coils and permanent magnets (PM) embedded in the stator. The electric machine contains both concentrated wound phase coils in dedicated slots and spoke-type permanent magnets solely in the stator. The spoke-type magnet arrangement achieves a high flux intensity even with low remanence non-rare earth permanent magnets. As the rotor has no active electromagnetic components, the risk for demagnetization is reduced and advanced cooling applied to the stator can enable high-speed operation. The principle of operation and polarity of the motor are investigated with a unique approach including analytical flux density analysis and piecewise computational modeling. A design optimization is performed for a 100kW motor at a speed of 3,000rpm, which is typical for industrial applications. The conflicting objectives of active material cost and motor losses are considered using both rare-earth and non-rare-earth ferrite PMs in the inner and outer rotor configurations of the proposed motor topology. Discussions on the trade-off between conflicting objectives, a specific EV motor design using ferrites, as well as alternative manufacturing, considering achievable slot fill factor (SFF) and choice of steel are also presented. Furthermore, an open-frame lab prototype (OFLP) of the proposed motor topology is constructed and tested to validate the principle of operation and design optimization approach, with due consideration to manufacturing.

Index Terms—Electric machine, synchronous motor, flux-intensifying topology, flux switching, flux modulation, variable flux, spoke permanent magnet, FEA, non-rare-earth.

I. INTRODUCTION

There is a need for continuous development of electrical machines to improve performance and enhance competitiveness [1]. The ongoing technological advancement is essential in driving innovation and meeting the growing demands of the evolving electric machine industry, which plays an important role in various sectors, such as energy generation, industrial applications, building appliances, and electrification of transportation [2].

The current paper proposes and reports on a special electric machine in which AC armature windings with concentrated toroidal coils, along with permanent magnets (PMs), are placed in the stator, and their combination with a reluctance

rotor is responsible for the excitation. The machine operates with a revolving fundamental field and belongs to the general class of hybrid synchronous, which also includes other topologies, such as for example those discussed in [3]. An alternator with dual sets of windings in the stator and a reluctance rotor, has been proposed in the 1950's and studied by Das Gupta, as part of his graduate studies research [4]. The research was contemporary with Rauch and Johnson's development and explanation, from an engineering-intuitive perspective, an alternator with AC windings and PMs in the stator, which they labeled as "flux switching" [5]. Das Gupta has continued analytical developments together with Dash in late 1960's [6], and in the 1990's machines with PMs in the stator have been proposed by Liao *et al.*, labeled as "doubly salient" PM [7], and by Deodhar *et al.*, as "flux reversal" doubly salient [8].

The development of such machines has been continuing, as summarized for example in a more recent review paper [9]. It should be noted that the term "flux switching" does not represent a complete definition, because in AC machines the magnetic flux is alternating and hence "switching". Therefore, typically the use of a reluctance or salient rotor needs to be additionally specified for clarification. These machines are not to be confused with the switched reluctance motors, which only have one set of windings in the stator and operate on different principles. The electronically controlled version of the switched reluctance motor has been introduced by Nasar in the late '60's [10], and this type of machines also benefited of developments over the years, as exemplified in a recent review paper [11].

The machine covered in the current paper employs in the stator a repetitive structure of circumferentially placed modules, each comprising a permanent magnet that is arranged radially and magnetized tangentially. Each stator module also includes a single coil belonging to one of the three-phase windings. The coils are concentrated and wound toroidally around the core, such that their magnetic flux axis is also tangentially oriented, similar to the magnets. The rotor has alternate protrusions creating a single flux barrier effect. The machine is operated with AC sinewave-regulated currents and may have some common features with what is typically informally labeled as "flux switching" machines, within, of

*Dr. Somasundaram Essakiappan and Dr. Madhav Manjrekar were with the QM Power, Inc., Kansas City, MO and are now with University of North Carolina at Charlotte, Charlotte, NC, USA.

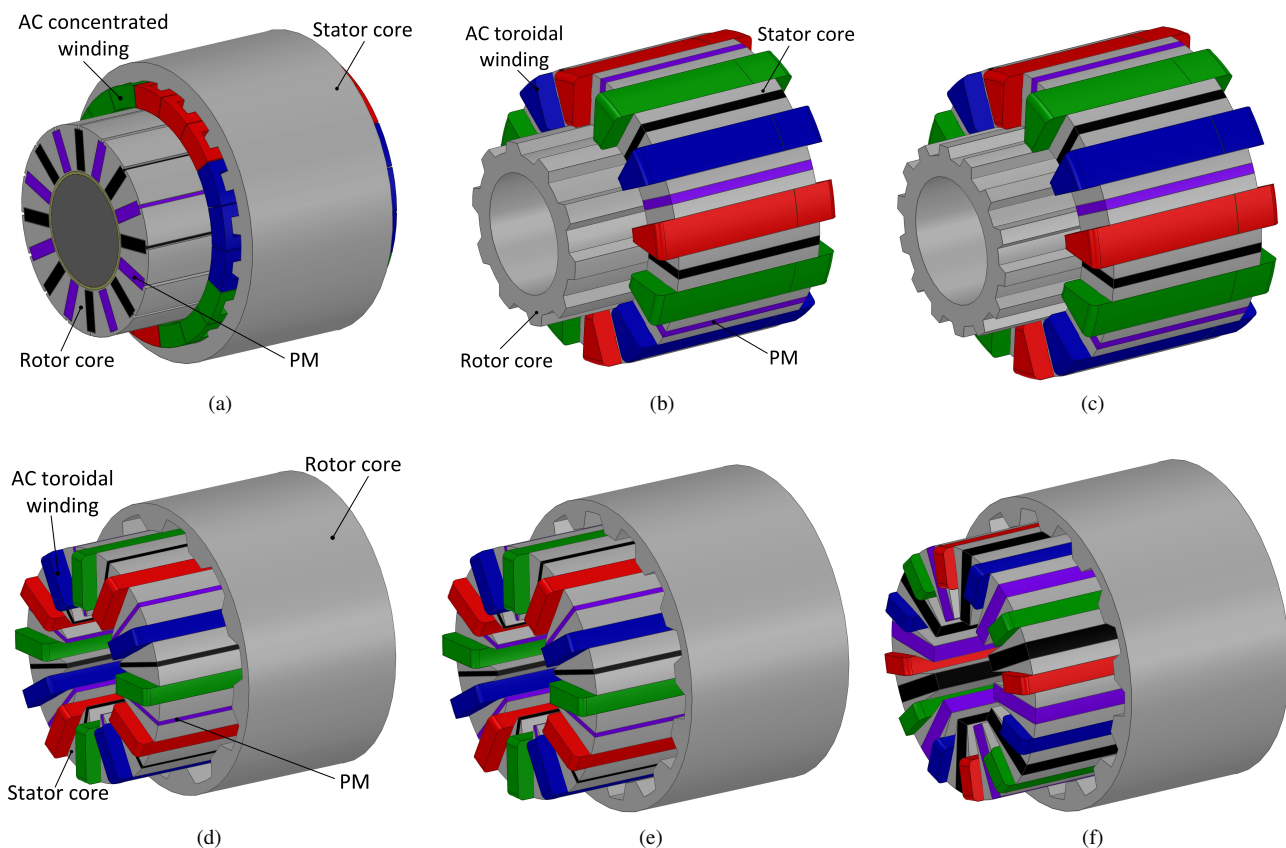


Fig. 1. Design evolution of high power density PM motor topologies from the (a) IPM spoke-type PM motor, to reluctance rotor motors with active stators having PMs and toroidal AC windings in (b) inner rotor configuration with 10 protrusions (-P), (c) inner rotor configuration with 14-P, (d) outer rotor configuration with 10-P, (e) outer rotor configuration with 14-P, and (f) outer rotor configuration with 14-P employing non-rare earth PMs.

course, the general class of synchronous hybrid excited to which it belongs.

This current paper expands on the authors' group research on the concept machine, which was recently studied for application in multi-MW direct drive generators by Mohammadi *et al.* [12], and for EV traction motors by Badewa *et al.* [13], and potential implementation in a dual-stage fault-tolerant electric machine concept for electric propulsion by Lewis *et al.* [14] in VTO DOE and NASA-funded projects. Each section brings substantial new contributions, as briefly described in the following. In the next section, possible arrangements with inner and outer stators, and with or without rare-earth PMs are introduced. To demonstrate that the hybrid synchronous excitation is provided not only by the stator components, but by their field interaction with a reluctance rotor of suitable polarity, a new analysis method considering the PMs, a two-part airgap permeance function, and the harmonics of the airgap field, is proposed and described in Section III. The comparative systematic optimal design of study from Section IV includes different main dimensions, polarities, NdFeB, and ferrite design versions with high flux concentration, identifies relative merits, and enables the generalization of the results. Manufacturing aspects are discussed with prototyping, testing,

and successful experimental validation in Section V, which is followed by a conclusion.

II. MOTOR TOPOLOGIES

In this machine, with implementation in inner and outer rotor configurations, the stator comprises multiple modules, each containing a PM and a single concentrated coil belonging to a phase winding as shown in Figs. 1b - f. The stator core is modular, with rectangular slots enabling the use of rectangular wire, leading to a high slot fill factor and low copper losses. The concentrated coils are toroidally wound, with compact axial ends, further contributing to reduced copper losses. The winding pattern follows the succession of the three phases around the stator circumference, and high fault tolerance is achieved by placing only one coil side in each slot. The PMs are also placed in the stator, in a radial position, with each two consecutive PMs magnetized tangentially in opposite directions.

The rotor does not include any active excitation components and has a laminated steel core of the reluctance-type with protrusions, the number and dimensions of which are coordinated with the stator characteristics. This simple rotor design allows for high-speed operation of the machine which is beneficial for range extension and overall high power density.

In the inner rotor configuration, as shown in Figs. 1b - c, the PM length is constrained by the rotor, necessitating an optimized split ratio between the rotor and stator for optimal performance. In contrast, the outer rotor configuration, illustrated in Figs. 1d - f, removes this constraint, allowing for longer PMs to be accommodated in the inner stator. This results in increased power density and maximization of flux intensification [15].

The associated high cost, material availability, and environmental sustainability of rare-earth PMs have always been a concern for PM-excited machines. The outer rotor configuration presents an opportunity for cost reduction by accommodating longer PMs made from less expensive and readily available materials. Lower-cost PMs, such as non-rare-earth, iron nitride, and ferrite types, can be used in greater quantities in the outer rotor configuration, shown in Fig. 1f, achieving competitive performance with rare-earth PM designs while reducing overall PM costs within the same volume [15], [16].

The subsequent sections will provide a more detailed analysis of the motor topology, its operation, and potential benefits. It is beneficial to mention that this motor topology is not without its challenges, such as eddy and supplementary losses due to significant magnetic field variations from open slots, as well as high common mode (CM) current and electromagnetic interference (EMI) issues associated with toroidal windings [17]–[19]. These challenges can be addressed through design improvements such as reduced slot openings, the use of Litz wire, and other advanced techniques [19], [20].

III. OPERATION AND ANALYSIS

In this section, a phenomenological approach is proposed to explain the operation of the proposed machine in its outer rotor configuration by studying the airgap flux, its modulation, and motor permeance. An examination of the airgap flux in this machine obtained through FEA simulation [21] gives insight into its operation, the geometric modulation of the primitive mmf produced by the PMs, as well as its polarity. The rotor and stator airgap permeance models are developed by studying their geometry and modulating effects through harmonic decomposition using Fourier series. Additionally, mathematical expressions for slot-pole and phase combinations are derived along with discussion on the flux concentration mechanism.

The original approach, combining a variety of techniques in a unique configuration, is used for the analysis of a machine with spoke-type PMs and stator-only excitation. The spoke-type topology allows for the maximization of PM utilization using the concept of flux concentration can be implemented similarly to the IPM motor shown in Fig. 1a and as previously exemplified in existing research and industrial projects, e.g. [22]–[24]. The explored machines, of which an example is provided in Fig. 1, are part of a general class of synchronous machines with stator-only excitation that have been referred to in recent literature as being of the "flux-switching" type and

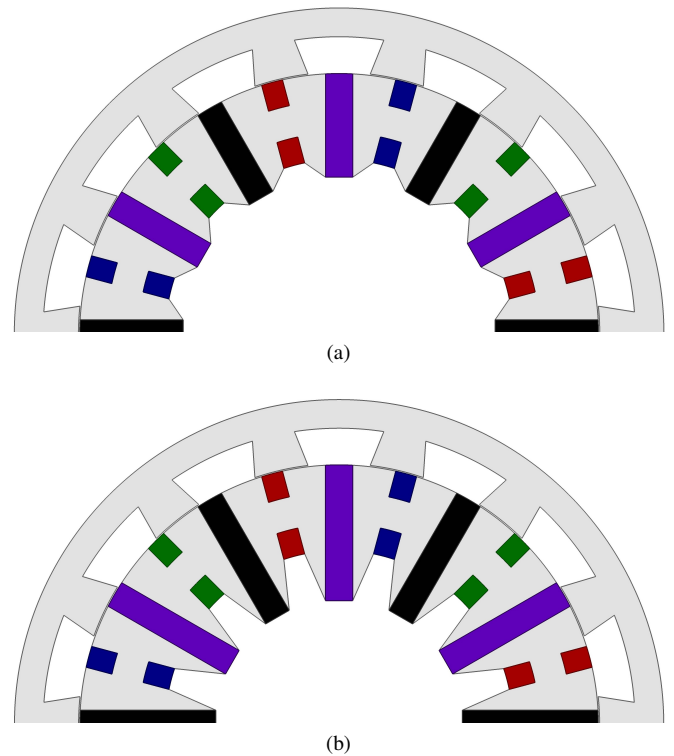


Fig. 2. Models of proposed motor topology in an outer rotor configuration showing changing PM radial length for flux concentration ratios of (a) 1.5, and (b) 2.0.

seek to leverage flux intensification for high power density [12], [13], [25].

The use of a solely active stator containing the PMs and toroidal AC windings reduces the risk of PM demagnetization and allows for advanced cooling concepts such as stator-only cooling, enabling high-speed operation. Possible implementations of state-of-the-art stator-only cooling include liquid cooling and stator-mounted air fin coolers [26], additively manufactured shaped and profiled windings with heat exchanger infill [27], and liquid pumps and microchannels [28]. The eventual choice of a cooling strategy would also be based on optimal design studies, with an example methodology as investigated by Fatemi *et. al* [29].

In the outer rotor configuration shown in Fig. 2, preliminary analysis indicates the potential for greater electromagnetic advantages compared to the inner rotor configuration through higher flux intensification from longer PMs, and larger possible airgap diameters [13]. In subsequent sections, systematic analysis and comparisons are detailed concerning the performance of the proposed synchronous machine in inner and outer rotor configurations.

A. Magnetic Field, Induced Voltage, and Polarity

The phenomenological breakdown of the principle of operation for the flux density in the airgap begins with the study of a computational variant with very thin magnets and no rotor protrusions. The PMs are modeled very thin to separate their effect, i.e. slot openings of the PMs, on the open circuit airgap

Table I
MOTOR PARAMETERS

| Description | Symbol | Unit |
|---|---------------|-------------------|
| Rotor outer diameter | OD_r | mm |
| Rotor inner diameter | ID_r | mm |
| Rotor pole pitch | τ_r | deg. |
| Number of rotor protrusions | N_{pr} | - |
| Stator outer diameter | OD_s | mm |
| Stator inner diameter | ID_s | mm |
| Stator pole pitch | τ_p | deg. |
| Number of phases | m | - |
| Number of armature winding slots | Z_l | - |
| Depth of the ac winding slot | h_{slot} | mm |
| Length of the ac winding slot | ℓ_{slot} | mm |
| PM length in the direction of magnetization | ℓ_{PM} | mm |
| PM height along the rotor radius | h_{PM} | mm |
| Airgap length | g | mm |
| Airgap diameter | D_g | mm |
| Stack length | ℓ_{stk} | mm |
| Rated current density | J | A/mm ² |

field and its harmonics. The open circuit radial component of flux density in the middle of the airgap for this model is depicted in Fig. 3a. The variation in flux density with a change in rotor angle can be represented by a square wave whose duty cycle is a function of PM width in the direction of magnetization and the stator pole pitch. The decomposition of this waveform shows harmonics of $k_p p_{PM}$, where k_p is an odd integer, and p_{PM} is the permanent magnets pole pair number, i.e. six in this example machine. Therefore, the mmf produced by the PMs only, F_{PM} , can be approximated with:

$$F_{PM}(\theta) = \sum_{v=1}^{\infty} \frac{F_{PM_{max}}}{(2v-1)} \sin[(2v-1)p_{PM}(\theta - \theta_o)], \quad (1)$$

where v is the harmonic order, and θ_o is the angular displacement from the stator reference point.

The addition of rotor protrusions to the computational model enables the confirmation of the equivalent number of poles in the machine, which varies from conventional motors due to the stator-only excitation. The altered model and normal component of the airgap flux density in open circuit condition considering the slot-less stator, PMs, and the castellated rotor is presented in Fig. 3b. It is observed that in this example machine, despite the 6-pole pair mmf, the dominant principle pole pair number is 14 consequent of the number of rotor protrusions N_{pr} , resulting in a 28-pole machine.

The stator permeance, Λ_s , considering the slots, PMs, and teeth positions relative to the reference axis, as shown in Fig. 4b can then be quantitatively summarized as:

$$\Lambda_s(\theta) = \begin{cases} \Lambda_{k_{min}}, & \theta \in (\theta - \frac{\beta_k}{2}, \theta + \frac{\beta_k}{2}) \\ \Lambda_{PM_{min}}, & \theta \in (\theta - \frac{\beta_{PM}}{2}, \theta + \frac{\beta_{PM}}{2}) \\ \Lambda_{st_{max}}, & \theta \in (\theta - \frac{\beta_{st}}{2}, \theta + \frac{\beta_{st}}{2}), \end{cases} \quad (2)$$

where θ is the angular displacement along the stator periphery, and β_k , β_{PM} , and β_{st} are the angular coordinates of stator slots, PMs, and teeth respectively. Minimum values of per-

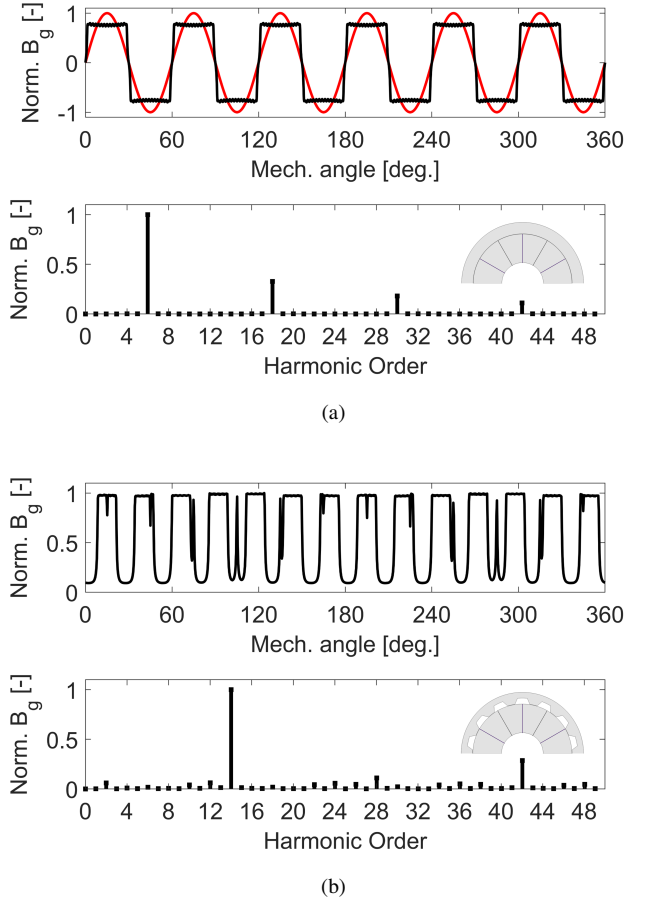


Fig. 3. Open circuit airgap flux and harmonic decomposition for computational models with (a) very thin magnets and the radial component with PMs only showing a 6-pole MMF, (b) very thin magnets with rotor protrusions and normal component indicating a 14 principal pole pairs corresponding to the number of rotor protrusions.

meance denoted by $\Lambda_{k_{min}}$ and $\Lambda_{PM_{min}}$ are obtained in the location of the slots and PMs respectively, while the maximum $\Lambda_{st_{max}}$ can be found in the stator teeth.

An unrolled linear equivalent geometry was developed as shown in Fig. 4b assuming an infinite permeability in the stator with the direction of the green arrow, and the dashed line as the center of the airgap. From this representation, the rotor airgap permeance per unit area can be approximated as a function, Λ_r , of the rotor moving in time, t , at a mechanical speed, ω , and starting at an initial position, θ_{r_0} , measured from the stator reference point. The resulting square wave function has minimum and maximum values dependent on the position of the rotor protrusions as shown in dotted lines in Fig. 4a.

The rotor permeance function can be expressed as:

$$\Lambda_r(\theta, t) = \Lambda_0 + \sum_{v=1}^{\infty} \Lambda_v \cos v [\theta - (\omega t + \theta_{r_0})], \quad (3)$$

$$\Lambda_0 = \mu_0 \left[\frac{1}{gMr} + \Gamma \left(\frac{1}{gMr} - \frac{1}{gmr} \right) \right], \quad (4)$$

$$\Lambda_v = \frac{2\mu_0}{v\pi} \left(\frac{1}{gMr} - \frac{1}{gmr} \right) \sin v\Gamma\pi, \quad (5)$$

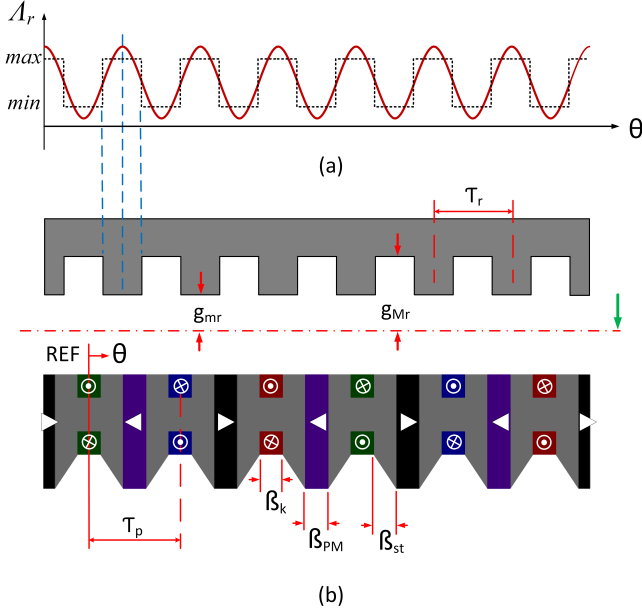


Fig. 4. (a) The rotor permeance square wave model and its fundamental component, and (b) a linear half-model of the proposed motor with a reference axis, airgap descriptions, stator, and rotor pole pitches, as well as angular coordinates of stator slots, teeth, and PMs. The horizontal dotted line is positioned at the center of the air gap.

where $(\omega t + \theta_{r_0})$ gives the angular displacement of the rotor from the stator reference point. The derived values of g and Γ consider appropriate Carter coefficients to account for slot openings and pole flux fringing effects.

The overall airgap permeance, $\Lambda_g(\theta, t)$, can then be obtained as:

$$\Lambda_g(\theta, t) = \Lambda_s(\theta) + \Lambda_r(\theta, t). \quad (6)$$

The open-circuit flux density in the machine airgap, $B_{g_o}(\theta, t)$, combines (1) and (6), the representations of the PM mmf and the airgap permeance, as:

$$B_{g_o}(\theta, t) = F_{PM}(\theta) \cdot \Lambda_g(\theta, t). \quad (7)$$

In this open circuit condition, the airgap flux due to the PMs, $\Psi_{PM}(\theta, t)$, can be obtained by integrating over the surface of the machine's airgap as:

$$\Psi_{PM}(\theta, t) = \int_S B_{g_o}(\theta, t) \cdot dS. \quad (8)$$

The back-EMF of this machine, $\mathcal{E}(\theta, t)$, is a function of the PM flux in the open circuit condition such that:

$$\mathcal{E}(\theta, t) = \frac{\partial \Psi_{PM}(\theta, t)}{\partial t}. \quad (9)$$

By examining the back-EMF obtained using FEA as given in Fig. 5, the motor polarity can be obtained from the period of the sinusoidal back-EMF waveform and speed of the motor. For this machine, at a speed of 3,000rpm, a period of 1.43ms

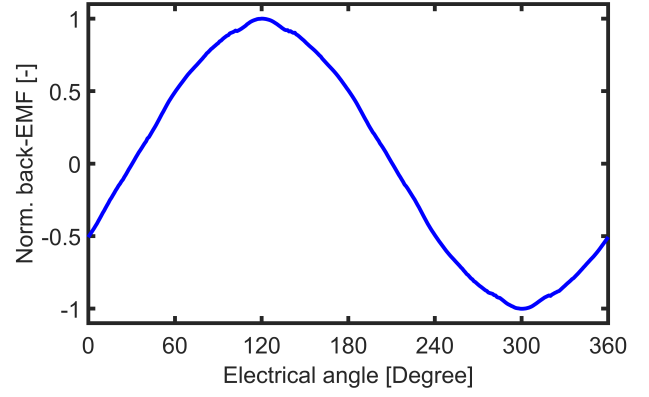


Fig. 5. Back-EMF of proposed motor with a period of 1.43ms at a speed of 3,000rpm; resultant of 28 electromagnetic/consequent poles.

is obtained corresponding to 14 pole-pairs, and 28 consequent pole motors.

B. Flux Concentration Analysis

The airgap flux density in the spoke-type PM arrangement of the studied machine can be mathematically expressed as follows:

$$B_{ag} = B_r \left(\frac{\pi D_g}{4k_\sigma N_{pr} h_{PM}} + \frac{2\mu_r g}{\ell_{PM}} \right)^{-1}, \quad (10)$$

where μ_r is the PM relative permeability, B_r the PM remanent flux density, and k_σ the rotor leakage coefficient, which can be adjusted to account for the saturation and slotting effects. The airgap flux density is directly related to PM remanent flux density, its length, and its height.

Considering the length of the PMs, a flux concentration ratio, ξ , can be defined as:

$$\xi = \frac{2h_{PM}}{\tau_p}. \quad (11)$$

With the spoke-type arrangement of PMs, the magnetic flux from two magnets contributes to the airgap magnetic flux in each pole, enhancing the overall magnetic field strength in line with expectations from previous work by Ionel *et al.* [23]. Models with flux concentration ratios of 1.5, and 2.0 are shown in Fig. 2 amongst a range of achievable ratios.

To determine the optimal flux concentration ratio, an “excitation goodness”, GD_{exc} , is defined as:

$$GD_{exc} = \frac{h_{PM} B_{PM} \ell_{stk}}{M_{PM}}, \quad (12)$$

where M_{PM} is the mass for each PM and suitable ratios are found for l_{PM} and h_{PM} . In line with expectations, increases in airgap flux density and flux concentration ratio improve excitation goodness but increase PM mass for the considered remanent flux densities.

To determine a suitable flux concentration ratio, another metric of performance is introduced known as the machine

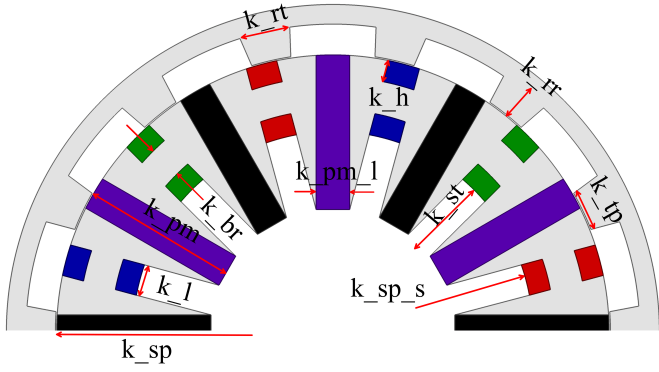


Fig. 6. Cross-sectional view of outer rotor design with 11 labeled geometric independent variables considered in the multi-objective optimization.

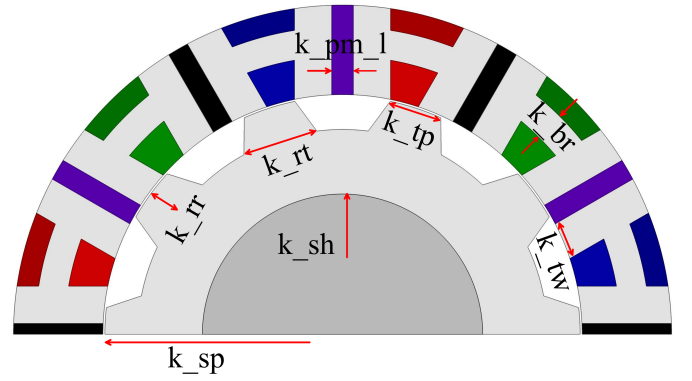


Fig. 7. Cross-sectional view of inner rotor design with 8 labeled geometric independent variables considered in the multi-objective optimization.

goodness, GD , which is defined as in [30]:

$$GD = \frac{T_{emg}}{\sqrt{P_{loss}}}, \quad (13)$$

where T_{emg} is the electromagnetic torque, and P_{loss} is the motor loss comprising components in the laminated core, and winding copper. The machine goodness was compared for potential designs with varying flux concentrations and PM width to stator pole pitch ratios. A flux concentration of two with a PM width ratio of 0.3 was optimally selected for an outer rotor configuration with the considered PM remanences of 0.4T and 0.8T similar to that discussed prior in [13].

IV. COMPARATIVE OPTIMIZATION STUDIES

A. Problem Formulation and Optimization

Manufacturing cost and efficiency are typically optimized for electric vehicle traction and propulsion motors while meeting necessary torque-speed requirements [29], [31]. Therefore, parametric models of the outer and inner rotor configurations of the proposed motor as shown in Figs. 6 and 7, with outermost diameters of 10" and 7", are analysed for an objective torque of 350Nm at a speed of 3,000rpm resulting in a 100kW motor which is typical for industrial applications [32], [33].

In the proposed motor, the outer rotor topology can concentrate flux and as such allows for utilization of lower-cost lower-remnance non-rare earth PMs such as ferrites. According to Rosu *et al* [1], active material cost (AMC) models can be established for machines with ferrite magnets (C_1), and NdFeB magnets (C_2), relative to per unit mass of laminated steel estimated as:

$$\begin{aligned} C_1 &= 5m_{PM} + 8m_{Cu} + 1m_{Fe}, \\ C_2 &= 65m_{PM} + 8m_{Cu} + 1m_{Fe}, \end{aligned} \quad (14)$$

where m_{Fe} is the mass of laminated steel, m_{Cu} mass of copper, and m_{pm} mass of permanent magnets.

The AMC objective formulation optimizes active mass by applying weighting factors accounting for production economics. Given the critical importance of cost, similar approaches have been used for design optimization aimed at the

Table II
INDEPENDENT VARIABLES AND THEIR RANGES FOR OPTIMIZATION OF THE INNER ROTOR DESIGN WITH NDFEB.

| Variable | Description | Min | Max |
|------------|--------------------------|------|------|
| k_{sp} | split ratio | 0.65 | 0.78 |
| k_{pm_l} | PM width ratio | 0.10 | 0.25 |
| k_{br} | bridge length ratio | 0.20 | 0.33 |
| k_{tw} | stator tooth width ratio | 0.20 | 0.30 |
| k_{sh} | shaft dia. ratio | 0.56 | 0.70 |
| k_{tp} | rotor pole top ratio | 0.48 | 0.72 |
| k_{rt} | rotor pole root ratio | 0.40 | 0.60 |
| k_{rr} | rotor pole depth ratio | 0.24 | 0.36 |

commercialization of IPM motors, as described by Fatemi *et al* [29] and Zhang *et al* [34], and DC-excited flux reversal motors for direct drive wind turbines by Kalengo *et al* [35]. For higher-performant higher-cost steel, for example, AK steel HF10, which is considered unless otherwise stated, a factor of 3 is considered the multiplier for m_{Fe} . Hence, the two concurrent optimization objectives in this study are to *minimize* the motor loss, F_1 , and active material cost, F_2 :

$$\begin{aligned} F_1 &= P_{loss} = P_{Fe} + P_{Cu}, \\ F_2 &= C_1 \text{ or } C_2. \end{aligned} \quad (15)$$

The objective function for motor loss was calculated as the sum of the variable and constant losses of the motor, where P_{Fe} represents the core loss (constant losses) and P_{Cu} represents the copper loss (variable losses) at a current density of 30A/mm² with anticipated liquid cooling. The objective function for AMC considers the cost of the stator core, rotor core, AC toroidal windings, and PMs.

In the developed parametric models, the inner and outer rotor topologies have 8 and 11 independent geometrical variables as described in Tables II and III. Due to non-linearities in the simulated responses of the proposed motor topology, it has been found that all variables play a significant role in its operation. Optimal ranges were therefore determined using analysis of data from sensitivity studies, response surface methodology (RSM), and box plot analysis with similar result

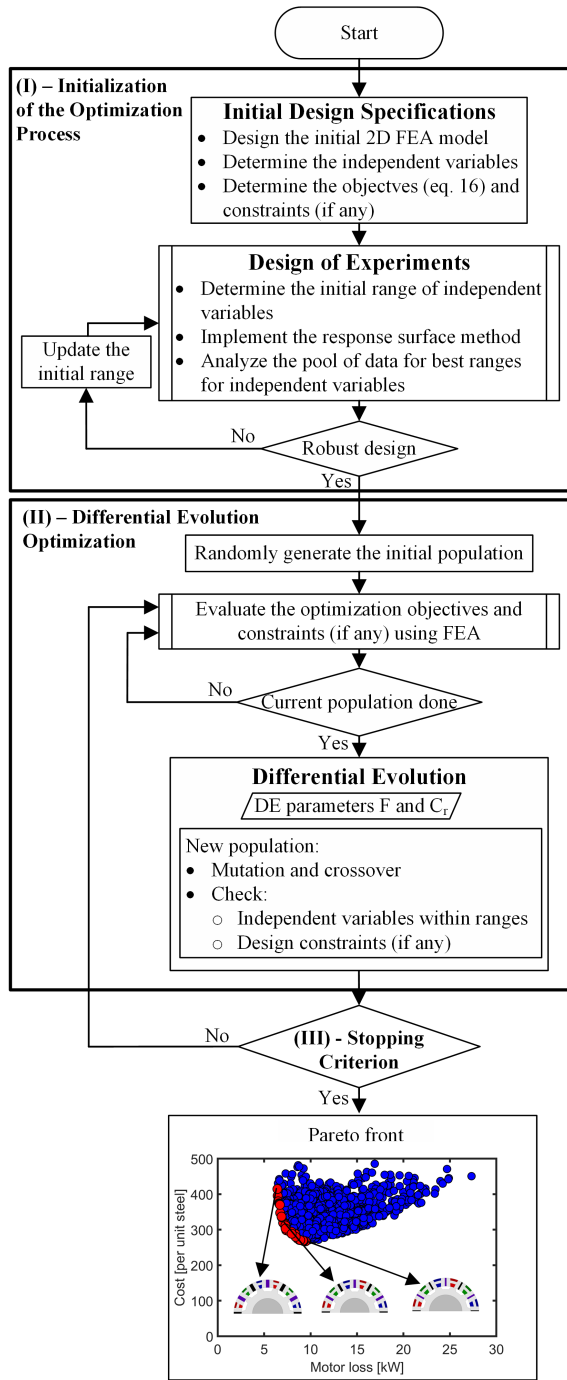


Fig. 8. The implemented two-level optimization algorithm is based on the differential evolution method using the design of experiments for initialization with an interior loop. The optimization results for the 7" OD I 10-P configuration are shown with the Pareto front designs in red. Cross-sections of selected designs from the Pareto show the change in the stator's PM, copper, and steel areas concerning cost and losses.

trends to those documented by the same group of authors in [12]. These studies were carried out for inner and outer rotor configurations having outermost diameters of 7" and 10" with 10 and 14 rotor protrusions employing NdFeB and ferrites and resultant optimization ranges are summarized in Tables II and

Table III
INDEPENDENT VARIABLES AND THEIR RANGES FOR OPTIMIZATION OF THE OUTER ROTOR DESIGN WITH NdFeB.

| Variable | Description | Min | Max |
|------------|------------------------|------|------|
| k_{sp} | split ratio | 0.70 | 0.85 |
| k_{pm} | PM length ratio | 1.00 | 1.20 |
| k_{pm_l} | PM width ratio | 0.15 | 0.25 |
| k_{br} | bridge length ratio | 0.20 | 0.40 |
| k_h | slot length ratio | 0.20 | 0.40 |
| k_l | slot width ratio | 0.20 | 0.40 |
| k_{tp} | rotor pole top ratio | 0.30 | 0.50 |
| k_{rt} | rotor pole root ratio | 0.30 | 0.50 |
| k_{rr} | rotor pole depth ratio | 0.40 | 0.60 |
| k_{sp_s} | stator split ratio | 0.40 | 0.50 |
| k_{st} | stator extension ratio | 0.20 | 0.35 |

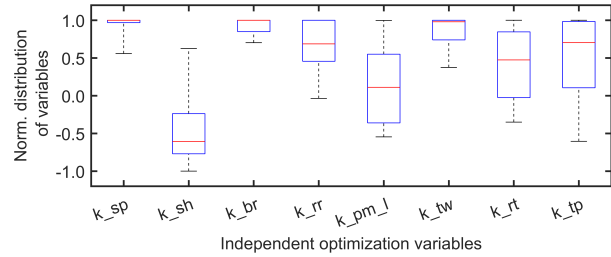


Fig. 9. The distribution of variables for optimum Pareto front designs for a 10" OD "I 10-P" configuration shows that variables responsible for the active stator cross-section favor the upper limits to reduce cost.

III to ensure robust FEA models and a wide optimization area.

The optimization process follows an extensively researched pattern employing differential evolution (DE) as depicted in the flowchart shown in Fig. 8 [1], [12], [36]. A two-pass study is used to ensure the rated torque of 350Nm at the rated speed of 3,000rpm is met by each design. Each design's torque is first obtained via FEA, and then the stack length is scaled to meet the required rated torque before evaluating it for the optimization objectives and other specified performance metrics. To improve the computational efficiency of the optimization, a hybrid stopping criterion is implemented that considers the convergence of the optimization algorithm either by meeting a maximum number of generations or when there is a minimal improvement in three representative points of the Pareto front for a few consecutive generations.

To further confirm that optimal ranges had been set for the independent variables, box plots showing the distribution of the independent variables of the Pareto designs, with one example shown in Fig. 9, were analyzed. In line with expectation, for the inner rotor configuration, the optimal designs favored the upper limits of k_{sp} , k_{br} , and k_{tw} in an attempt to reduce the cost and losses of the active stator in line with optimization objectives.

B. Results and Discussion

Following optimization of the inner and outer rotor topologies with specifics described in the previous subsection, the

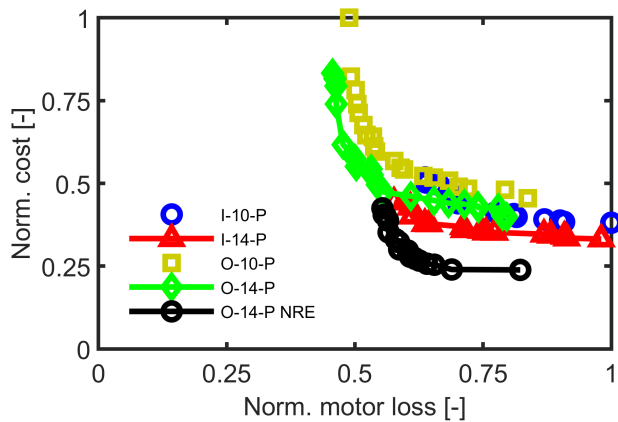


Fig. 10. Pareto front designs obtained from optimization of normalized AMC and motor losses for 10'' OD, having inner (I) or outer (O) rotor configurations with rare-earth NdFeB or non-rare earth ferrite (NRE) having 10 (10-P) or 14 (14-P) rotor protrusions. The normalization bases for all 10'' OD designs for cost and losses are 567 per unit steel and 9.0kW respectively.

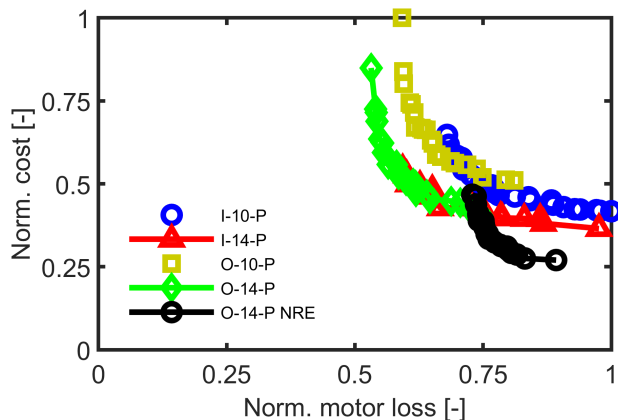


Fig. 11. Pareto front designs obtained from optimization of AMC and motor losses for 7'' OD. The normalization bases for the cost and losses are 640 per unit steel and 9.5kW respectively.

Pareto front designs for inner (I) and outer (O) rotor topologies with rare-earth NdFeB or non-rare earth ferrite (NRE) having 10 (10-P) or 14 (14-P) rotor protrusions for outermost diameters of 10'' and 7'' are shown in Figs. 10 and 11 respectively. Irrespective of the selected diameter, the designs employing non-rare earth ferrites (NRE) come to have the lowest cost in line with expectations since they can use larger PMs without significantly impacting the overall cost.

The outer rotor (O) designs can be seen to generally favor higher cost and lower loss as compared to the inner rotor (I) designs and this can be attributed to their geometry naturally tending toward longer PMs for flux intensification and a shorter stack length. Also, comparing the 10'' and 7'' OD designs, the AMC increases with a decrease in diameter as expected since torque increases with airgap diameter, so shorter stack lengths are required. The 10'' OD outer rotor designs due to the availability of a larger cross-sectional area

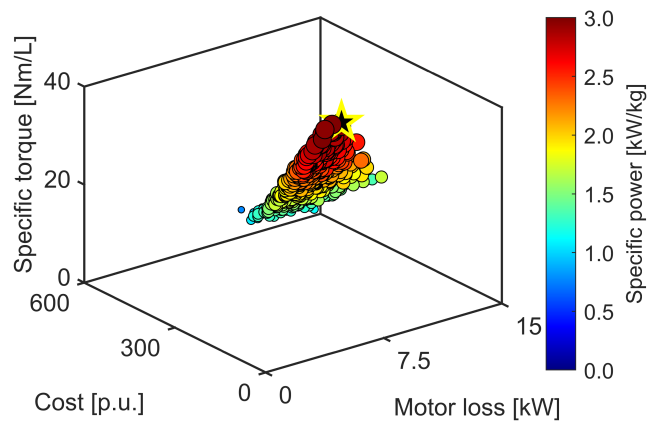


Fig. 12. Optimization results for the 10'' O-14-P NRE configuration operating at 3,000rpm showing high torque density, low active mass, and low cost can be achieved with the selected design marked with a black star.

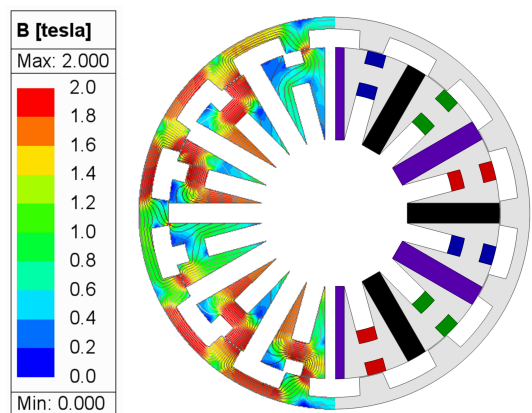


Fig. 13. The cross-sectional view of the selected cost-effective high torque density "best" design OR-NRE D1.

for flux intensification with longer PMs can be seen to embrace the use of ferrites more cost-effectively and may compete favorably with state-of-the-art motors using rare-earth PMs, especially at larger diameters. Also, between the 14-P and 10-P configurations, the lesser polarity designs generally did not fare badly and provided competitive performance in terms of cost and losses.

C. Specific EV Motor Design using Ferrites

Conflicting objectives of cost and motor losses result in design selection depending on priority within the intended use case. An outer rotor topology employing ferrites may be a cost-effective solution for industrial applications as summarized in Figs. 10 and 11, especially at larger diameters. Considering typical light and medium-duty EV applications, a 10'' OD "O-14-P NRE" configuration is proposed with design selection considering other critical factors such as torque density, torque ripple, and weight.

A plot of the optimization results for the 10'' OD designs employing ferrites in Fig. 12 shows that the highest torque density designs can be obtained without sacrificing cost and

Table IV
PERFORMANCE SPECIFICATIONS FOR OR-NRE D1

| Parameter | Value | Unit |
|--|-------|------|
| Peak torque at 30A/mm ² | 350 | Nm |
| Continuous torque at 10A/mm ² | 156 | Nm |
| Max. power | 100 | kW |
| Base speed | 3,000 | rpm |
| Emag eff. at peak torque | 92.8 | % |
| Emag eff. at continuous torque | 96.8 | % |
| Rotor OD | 10.0 | inch |
| Stack length | 6.6 | inch |
| Total active mass | 35 | kg |

active mass. The specific power, a function of active mass, is especially crucial in applications where weight is a major concern, such as electric vehicles (EVs). It can be observed that designs with lower active mass—and thus higher specific power—also tend to occupy less volume. The cross-section of an example selected cost-effective high torque density design “OR-NRE D1” is shown in Fig. 13 with its performance summarized in Table. IV. With a peak torque of 350Nm, the selected design has a torque ripple of approximately 5% which is considered satisfactory for typical applications and can be further improved through optimization or rotor shaping techniques [37]. With a specific torque of 10Nm/kg, this design competes well with state-of-the-art traction motors with publicly available 9 - 15Nm/kg performance estimates as reported in [24].

V. MANUFACTURING CONSIDERATIONS, PROTOTYPING, AND EXPERIMENTATION

A. Manufacturing Options

Considering manufacturing in the proposed motor topologies, the use of toroidal windings in an active stator provides the advantages of shortened end turns for reduced losses, the possibility of stator-only cooling, as well as potentially shorter coils as compared to other winding types depending on the aspect ratio of the machine. This winding type is also suitable for low torque ripple applications advantageous in EVs and aerospace applications with the downside of increased common mode (CM) current and EMI issues which can be managed through design [19].

In the previous sections, analysis has been carried out considering the highest performant steel and latest winding technology for high SFF as documented in [38], [39]. In this section, analysis based on the scaled performance of the 7" OD optimization resultant designs is carried out with a view to manufacturing/prototyping considering a lower-cost steel and a base slot fill factor of 0.4 which is typical, especially for hand-wound prototypes.

Considering a lower SFF of 0.4, the performance of the Pareto designs as in Fig. 14a shows an increase in cost as longer stack and PM lengths compensate for the reduced SFF. Also, the motor losses are reduced since the copper losses dominate at this rated current density and speed. For lower-cost M19-29G steel, the performance of the obtained Pareto

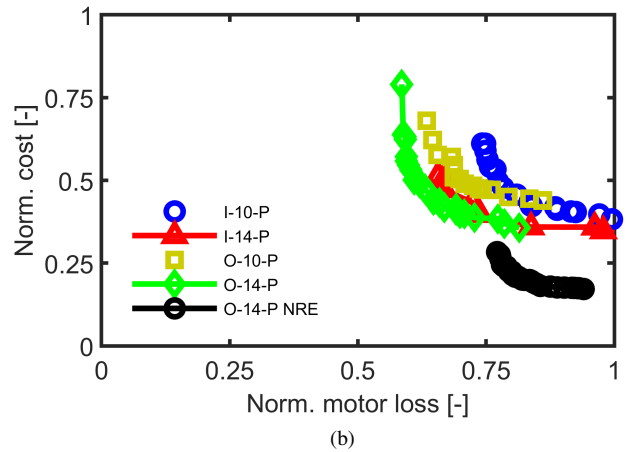
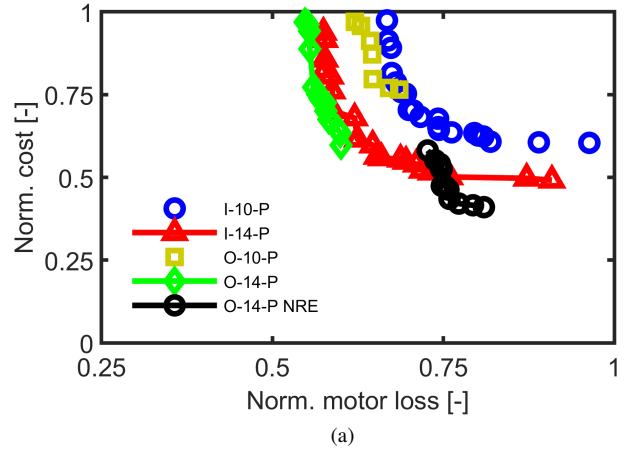


Fig. 14. Performance evaluation of 7" OD optimization result designs showing Pareto fronts considering only (a) a lower SFF of 0.4, and (b) the use of lower-cost steel M19-29G

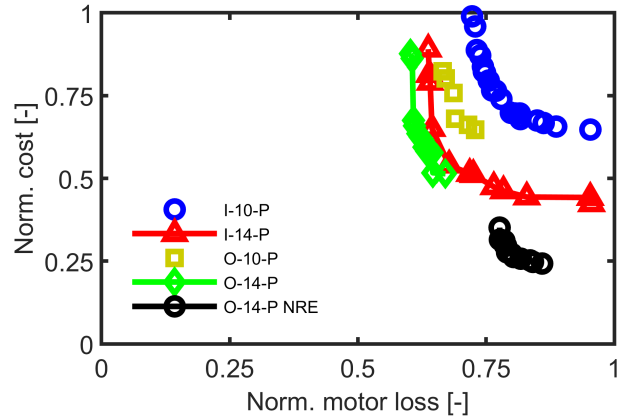
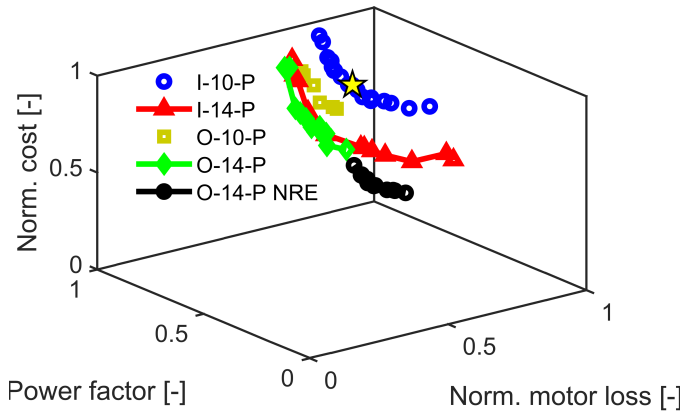
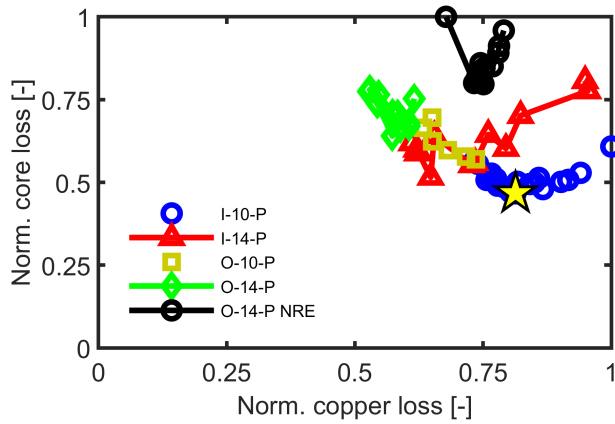


Fig. 15. Performance evaluation of 7" OD optimization result designs showing Pareto fronts considering a lower SFF of 0.4 and using lower-cost steel M19-29G.

as shown in Fig. 14b indicates that the cost is not significantly impacted since there is a counter-balance between increased stack length and lower steel cost.



(a)



(b)

Fig. 16. Performance evaluation of 7" OD Pareto front designs using M19-29G steel and an SFF of 0.4 considering (a) power factor which improves with cost, and (b) separation of losses. The selected design for prototyping is marked with a star having the lowest value of core loss.

With a SFF of 0.4 and M19-29G steel, the performance of the obtained Pareto designs is shown in Fig. 15, with a further evaluation of their power factors and loss components as in Fig. 16. While the various configurations compete favorably in terms of power factor with compromises in cost, the 10-P configurations have lower core losses in line with expectations, especially in the I-10-P configuration. For the proposed prototype, the selected design indicated with a star in Fig. 16 and having a cross-section as shown in Fig. 7 has a competitive compromise between power factor and cost, and the least value of core loss amongst all the designs. This low core loss value makes it suitable for operation at higher speeds since core losses scale with the square of frequency.

B. Prototype and Experimentation

To further the electromagnetic characterization of the proposed topology including the theoretical development to explain operation as a synchronous machine, the configuration with 10 rotor protrusions, "I-10-P" was selected for prototyping. The inner (I) rotor configuration is believed to win

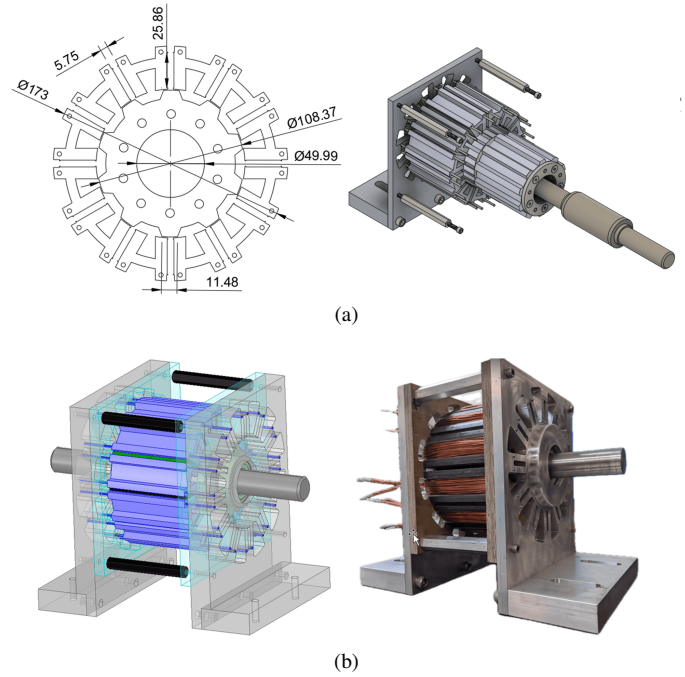


Fig. 17. Experimental development of the selected motor design showing: (a) dimensioned component and assembly drawings, and (b) CAD model and constructed open-frame laboratory prototype (OFLP) of the 7" OD, 10-protrusion motor with a 4" stack length.

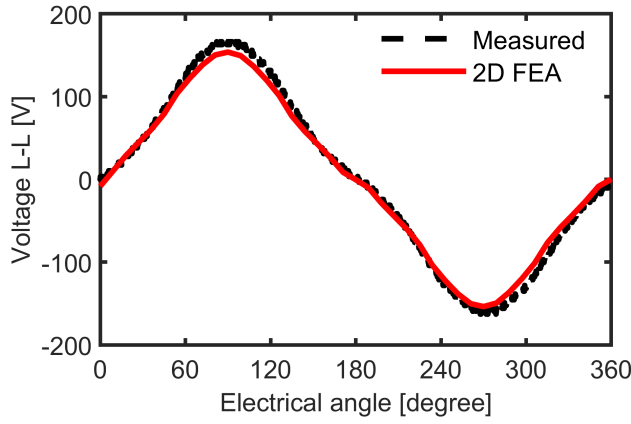
Table V
FEA AND EXPERIMENTAL VALUES OF CORE LOSS AT OPEN-CIRCUIT FOR THE MODEL AND OFLP. AN EXPONENTIAL INCREASE IN LOSS CAN BE SEEN WITH INCREASED POLARITY AND SPEED.

| Speed | FEA | Exp. | Error | Est. |
|-------|-------|-------|-------|-------|
| [rpm] | 10-P | 10-P | [%] | 14-P |
| 1,000 | 70.2 | 83.0 | 15.4 | 162.7 |
| 1,500 | 129.5 | 141.6 | 8.5 | 277.4 |
| 2,000 | 204.6 | 206.0 | 0.7 | 403.7 |
| 2,500 | 295.2 | 292.8 | 0.8 | 574.0 |
| 3,000 | 401.4 | 368.9 | 8.8 | 723.0 |

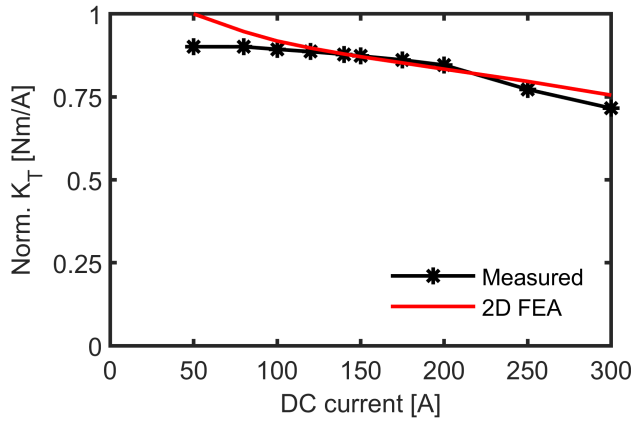
with considerations to thermal and typical implementation with non-moving external parts and stator directly attached to the outer frame.

An open-frame lab prototype (OFLP) was constructed as shown in Fig. 17, with a 4" stack length, having eight N42 grade NdFeB PM segments stacked in each of the PM slots. With natural cooling, the OFLP was experimentally characterized through a combination of static and rotational experiments to a static torque of 60Nm and a speed of 3,000rpm. A comparison of the experimental and FEA results in Figs. 18 and 19 for the line-to-line back-EMF, static torque constant κ_T , and variation of static torque with rotor position shows good agreement between experimental and 2D FEA results.

Core losses were measured at open-circuit and a good correlation was obtained compared to the FEA results, as detailed in Table V. The measured values from the prototype are also scaled to obtain an estimate considering 14-P to show



(a)



(b)

Fig. 18. Experimental and FEA results for (a) line-to-line back EMF of the prototype for one electric period at a rotor speed of 3,500rpm, which demonstrates good agreement between the measurement and simulation, and (b) normalized torque constant κ_T with a base value of 0.33 showing good correlation between prototype and model.

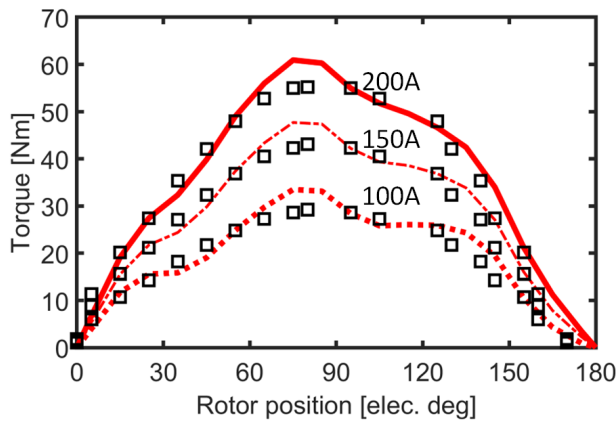


Fig. 19. Experimental (discrete rectangles) and FEA (lines) results for static torque vs rotor position.

the exponential effect of increased polarity on core losses with increasing speed. The absolute percentage difference between

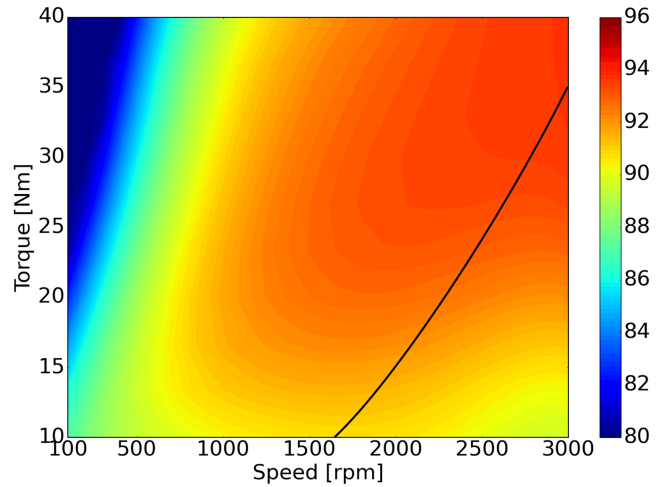


Fig. 20. The efficiency map for the prototype machine plotted together with the curve corresponding to an 11kW rated pump at full speed.

the simulated and experimental core loss values is below 10% for the key speed ranges analyzed, with a slightly higher discrepancy at the lowest speed, which can be attributed to the typical challenges of low-speed measurements, such as equipment sensitivity, noise, and thermal effects. The efficiency map of the prototype machine was derived using experimentally measured torque and power losses as shown in Fig. 20 plotted together with the curve corresponding to an 11kW rated pump at full speed.

The investigated motor topology has been proposed for applications in multi-MW direct-drive generators in wind turbines, EVs, and implementation in a dual-stage fault-tolerant electric machine concept for electric propulsion in VTO DOE and NASA-funded projects [12], [14], [40]. Ongoing research focuses on exploring the fault-tolerant operation of this machine topology, innovative integrated cooling strategies, and its synchronization within a dual-stage machine arrangement.

VI. CONCLUSION

The theory of operation and systematic optimization were developed for a specialized electric machine topology that employs toroidally wound coils, permanent magnets, and a reluctance rotor, and these were experimentally validated. In the investigated topology, localizing active components to the stator allows for easier heat dissipation with the possible implementation of advanced stator-only cooling methods, increasing potential efficiency and reliability. In the outer rotor configuration, the machine can have a larger airgap diameter, larger stator coils, and longer PMs resulting in greater average torque and power density than an inner rotor configuration. Effective implementation of flux-focusing enables the use of cheaper non-rare PM materials such as ferrites, reducing machine cost and environmental impact while achieving competitive performance.

A phenomenological approach was developed to analyze the principle of operation for the proposed machine which was

used for the systematic design of key motor parameters. A mixture of piece-wise computational and analytical modeling allows for the characterization of PM mmf and confirmation of the fact that irrespective of polarity, the principal pole pair number is a function of the number of rotor protrusions, i.e., 14 rotor protrusions result in a 14-pole pair machine. Design for flux concentration was also discussed while considering the potential impact on machine goodness or the ratio of torque output to the square root of losses.

Systematic comparison for both inner and outer rotor configurations based on cost and losses indicated that having a 14-protrusion rotor has the advantage for specific power, especially in the outer rotor configuration while the 10-protrusion rotor design has advantages in terms of power factor and losses, especially at high operating speeds. Overall, the electromagnetic advantages of the outer rotor configuration may not be big enough to justify the complexity of integrating an outer rotor structure in an application dominated by inner rotor constructions.

ACKNOWLEDGMENT

This paper is based upon research sponsored by QM Power, Inc. The support of ANSYS Inc., and University of Kentucky the L. Stanley Pigman Chair in Power Endowment is also gratefully acknowledged.

REFERENCES

- [1] M. Rosu, P. Zhou, D. Lin, D. M. Ionel, M. Popescu, F. Blaabjerg, V. Rallabandi, and D. Staton, *Multiphysics simulation by design for electrical machines, power electronics and drives*. John Wiley & Sons, 2017.
- [2] B. Sarlioglu, C. T. Morris, D. Han, and S. Li, "Driving toward accessibility: A review of technological improvements for electric machines, power electronics, and batteries for electric and hybrid vehicles," *IEEE Industry Applications Magazine*, vol. 23, no. 1, pp. 14–25, 2017.
- [3] Y. Amara, H. B. Ahmed, and M. Gabsi, *Hybrid Excited Synchronous Machines: Topologies, Design and Analysis*. John Wiley & Sons, 2023, ISBN: 9781786306852.
- [4] A. K. Das Gupta, *An analysis of one type of inductor alternator*. University of Wisconsin-Madison, 1958.
- [5] S. E. Rauch and L. J. Johnson, "Design principles of flux-switch alternators [includes discussion]," *Transactions of the American Institute of Electrical Engineers. Part III: Power Apparatus and Systems*, vol. 74, no. 3, pp. 1261–1268, 1955.
- [6] P. K. Dash and A. K. Das Gupta, "Inductance coefficients of three-phase inductor alternators: Part I - analytical study," *IEEE Transactions on Power Apparatus and Systems*, vol. PAS-88, no. 11, pp. 1725–1730, 1969.
- [7] Y. Liao, F. Liang, and T. Lipo, "A novel permanent magnet motor with doubly salient structure," *IEEE Transactions on Industry Applications*, vol. 31, no. 5, pp. 1069–1078, 1995.
- [8] R. Deodhar, S. Andersson, I. Boldea, and T. Miller, "The flux-reversal machine: a new brushless doubly-salient permanent-magnet machine," *IEEE Transactions on Industry Applications*, vol. 33, no. 4, pp. 925–934, 1997.
- [9] H. Chen, A. M. El-Refai, and N. A. O. Demerdash, "Flux-switching permanent magnet machines: A review of opportunities and challenges—part I: Fundamentals and topologies," *IEEE Transactions on Energy Conversion*, vol. 35, no. 2, pp. 684–698, 2020.
- [10] S. Nasar, "DC-switched reluctance motor," in *Proceedings of the institution of electrical engineers*, vol. 116, no. 6. IET, 1969, pp. 1048–1049.
- [11] M. Abdalmagid, E. Sayed, M. H. Bakr, and A. Emadi, "Geometry and topology optimization of switched reluctance machines: A review," *IEEE Access*, vol. 10, pp. 5141–5170, 2022.
- [12] A. Mohammadi, O. A. Badewa, Y. Chulaee, D. D. Lewis, S. Essakiappan, M. Manjrekar, and D. M. Ionel, "Design optimization of a direct-drive wind generator with a reluctance rotor and a flux intensifying stator using different PM types," *IEEE Transactions on Industry Applications*, pp. 1–10, 2024.
- [13] O. A. Badewa, A. Mohammadi, D. D. Lewis, D. M. Ionel, S. Essakiappan, and M. Manjrekar, "Optimization of an electric vehicle traction motor with a PM flux intensifying stator and a reluctance outer rotor," in *2023 IEEE Transportation Electrification Conference & Expo (ITEC)*, 2023.
- [14] D. D. Lewis, O. A. Badewa, A. Mohammadi, M. Vatani, and D. M. Ionel, "Fault tolerant electric machine concept for aircraft propulsion with PM rotor and DC current stator dual-stage excitation," in *2023 12th International Conference on Renewable Energy Research and Applications (ICRERA)*, 2023, pp. 607–611.
- [15] O. A. Badewa and D. M. Ionel, "Comparative analysis of motors with inner and outer reluctance rotors and PM stators," in *2024 IEEE Transportation Electrification Conference and Expo (ITEC)*, 2024, pp. 1–6.
- [16] A. Al-Qarni and A. El-Refai, "Optimum rotor design for rare-earth free high performance traction applications interior permanent magnet motors enabled by iron nitride permanent magnet," in *2023 IEEE International Electric Machines & Drives Conference (IEMDC)*, 2023, pp. 1–7.
- [17] N. Taran, D. M. Ionel, V. Rallabandi, G. Heins, and D. Patterson, "An overview of methods and a new three-dimensional FEA and analytical hybrid technique for calculating AC winding losses in PM machines," *IEEE Transactions on Industry Applications*, vol. 57, no. 1, pp. 352–362, 2021.
- [18] A. Fatemi, D. M. Ionel, N. A. O. Demerdash, D. A. Staton, R. Wrobel, and Y. C. Chong, "Computationally efficient strand eddy current loss calculation in electric machines," *IEEE Transactions on Industry Applications*, vol. 55, no. 4, pp. 3479–3489, 2019.
- [19] S. Lee, W. Lee, M. Liu, and B. Sarlioglu, "High-frequency motor impedance analysis and CM current estimation of electric motors with concentrated and toroidal windings," *IEEE Transactions on Transportation Electrification*, pp. 1–1, 2024.
- [20] M. Popescu and D. G. Dorrell, "Proximity losses in the windings of high speed brushless permanent magnet AC motors with single tooth windings and parallel paths," *IEEE Transactions on Magnetics*, vol. 49, no. 7, pp. 3913–3916, 2013.
- [21] *Ansys® Electronics, version 23.2, 2023, ANSYS Inc.*
- [22] D. Ionel, J. Eastham, and T. Betzer, "Finite element analysis of a novel brushless DC motor with flux barriers," *IEEE Transactions on Magnetics*, vol. 31, no. 6, pp. 3749–3751, 1995.
- [23] D. Ionel, D. Jackson, G. Starr, and A. Turner, "Permanent magnet brushless motors for industrial variable speed drives," in *2002 International Conference on Power Electronics, Machines and Drives (Conf. Publ. No. 487)*, 2002, pp. 650–654.
- [24] A. Fatemi, D. M. Ionel, M. Popescu, Y. C. Chong, and N. A. O. Demerdash, "Design optimization of a high torque density spoke-type PM motor for a formula E race drive cycle," *IEEE Transactions on Industry Applications*, vol. 54, no. 5, pp. 4343–4354, 2018.
- [25] P. Han, M. G. Kesgin, D. M. Ionel, R. Gosalia, N. Shah, C. J. Flynn, C. S. Goli, S. Essakiappan, and M. Manjrekar, "Design optimization of a very high power density motor with a reluctance rotor and a modular stator having PMs and toroidal windings," in *2021 IEEE Energy Conversion Congress and Exposition (ECCE)*. IEEE, 2021, pp. 4424–4430.
- [26] D. Konovalov, I. Tolstorebrov, T. M. Eikevik, H. Kobalava, M. Radchenko, A. Hafner, and A. Radchenko, "Recent developments in cooling systems and cooling management for electric motors," *Energies*, vol. 16, no. 19, p. 7006, 2023.
- [27] N. Simpson, G. Yiannakou, H. Felton, J. Robinson, A. Arjunan, and P. H. Mellor, "Direct thermal management of windings enabled by additive manufacturing," *IEEE Transactions on Industry Applications*, vol. 59, no. 2, pp. 1319–1327, 2023.
- [28] D. Talebi, C. Wiley, S. V. Sankarraman, M. C. Gardner, and M. Benedict, "Design of a carbon fiber rotor in a dual rotor axial flux motor for electric aircraft," *IEEE Transactions on Industry Applications*, vol. 60, no. 5, pp. 6846–6855, 2024.
- [29] A. Fatemi, D. M. Ionel, N. A. O. Demerdash, and T. W. Nehl, "Optimal design of IPM motors with different cooling systems and winding configurations," *IEEE Transactions on Industry Applications*, vol. 52, no. 4, pp. 3041–3049, 2016.

- [30] N. Taran, G. Heins, V. Rallabandi, D. Patterson, and D. M. Ionel, "Evaluating the effects of electric and magnetic loading on the performance of single- and double-rotor axial-flux PM machines," *IEEE Transactions on Industry Applications*, vol. 56, no. 4, pp. 3488–3497, 2020.
- [31] M. G. Kesgin, P. Han, N. Taran, and D. M. Ionel, "Optimal study of a high specific torque vernier-type axial-flux PM machine with two different stators and a single winding," in *2020 IEEE Energy Conversion Congress and Exposition (ECCE)*, 2020, pp. 4064–4067.
- [32] M. Kimiabeigi, J. D. Widmer, R. Long, Y. Gao, J. Goss, R. Martin, T. Lisle, J. M. Soler Vizan, A. Michaelides, and B. Mecrow, "High-performance low-cost electric motor for electric vehicles using ferrite magnets," *IEEE Transactions on Industrial Electronics*, vol. 63, no. 1, pp. 113–122, 2016.
- [33] X. Sun, Z. Shi, G. Lei, Y. Guo, and J. Zhu, "Analysis and design optimization of a permanent magnet synchronous motor for a campus patrol electric vehicle," *IEEE Transactions on Vehicular Technology*, vol. 68, no. 11, pp. 10535–10544, 2019.
- [34] P. Zhang, D. M. Ionel, and N. A. O. Demerdash, "Saliency ratio and power factor of IPM motors optimally designed for high efficiency and low cost objectives," in *2014 IEEE Energy Conversion Congress and Exposition (ECCE)*, 2014, pp. 3541–3547.
- [35] K. Kalengo, M. Bharathi, U. B. Akuru, and O. M. Popoola, "Sizing and comparative performance evaluation of a 5 kW DC-Excited flux reversal direct-drive wind generator," in *2024 32nd Southern African Universities Power Engineering Conference (SAUPEC)*, 2024, pp. 1–6.
- [36] N. Taran, V. Rallabandi, G. Heins, and D. M. Ionel, "Systematically exploring the effects of pole count on the performance and cost limits of ultrahigh efficiency fractional hp axial flux PM machines," *IEEE Transactions on Industry Applications*, vol. 56, no. 1, pp. 117–127, 2020.
- [37] J. Qi, Z. Q. Zhu, L. Yan, G. W. Jewell, C. Gan, Y. Ren, S. Brockway, and C. Hilton, "Suppression of torque ripple for consequent pole PM machine by asymmetric pole shaping method," *IEEE Transactions on Industry Applications*, vol. 58, no. 3, pp. 3545–3557, 2022.
- [38] A. Kampker, H. H. Heimes, B. Dorn, F. Brans, and C. Stäck, "Challenges of the continuous hairpin technology for production techniques," *Energy Reports*, vol. 9, pp. 107–114, 2023.
- [39] A. Selema, M. N. Ibrahim, and P. Sergeant, "Advanced manufacturability of electrical machine architecture through 3D printing technology," *Machines*, vol. 11, no. 9, 2023.
- [40] C. S. Goli, M. G. Kesgin, P. Han, D. M. Ionel, S. Essakiappan, J. Gafford, and M. D. Manjrekar, "Analysis and design of an electric machine employing a special stator with phase winding modules and PMs and a reluctance rotor," *IEEE Access*, vol. 12, pp. 9621–9631, 2024.



Oluwaseun A. Badewa (Graduate Student Member, IEEE) received the B.Sc. degree from ATBU, Bauchi, Nigeria, and the M.Sc. degree from CAU, Kiel, Germany both in Electrical engineering. From 2016 to 2020, he worked as a Senior Electrical engineer with DORCL, Nigeria specialized in electrical design and detailed engineering, and commissioning for petrochemical complexes. He is currently working toward the Ph.D. degree with SPARK Laboratory, Department of Electrical and Computer Engineering, University of Kentucky, Lexington, KY, USA. He was the co-recipient of the Best Paper Award at the 2022 IEEE International Conference on Renewable Energy Research and Applications (ICRERA) with a paper on multi-MW direct-drive wind-turbine generators employing a flux intensifying PM stator and reluctance rotor novel topology. At UK, he has been working as a Research Assistant with research interests in electric machines and power electronic drives.



Ali Mohammadi (Graduate Student Member, IEEE) received the B.Sc. and M.Sc. degrees from Babol Noshirvani University of Technology (BNUT), Iran, in 2016 and 2020, respectively. He is currently pursuing his Ph.D. at the SPARK Laboratory, Department of Electrical and Computer Engineering, University of Kentucky, Lexington, KY, USA. His research focuses on renewable energies, transportation electrification, advanced electromagnetic finite element analysis, and the innovative design and optimization of electric machines, motor drives, and power electronics. He

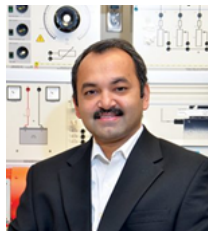
has been the recipient of several accolades, including the IEEE Transactions on Energy Conversion journal Best Paper Award and multiple IEEE conference Best Paper Awards, for his dedication to specialty electric machines.



Donovin D. Lewis (Graduate Student Member, IEEE) received the B.Sc. degree in electrical engineering in 2021 from the University of Kentucky, Lexington, KY, USA, where he is working toward the Ph.D. degree with the SPARK Laboratory, Department of Electrical and Computer Engineering. He is also a remote research collaborator with Oak Ridge National Laboratory, and a summer visitor with the University of Oxford, Oxford, England. During his undergraduate studies, he was a William C. Parker Scholar, a NASA REU student, a recipient of the IEEE PES Plus Scholarship, and the Chief Electrical Engineer of the 2021 U.S. National Champion University of Kentucky Solar Car Team. He is currently a National Science Foundation (NSF) Graduate Research Fellow, was a University of Kentucky Otis A. Singletary Graduate Fellow, and has been recognized by the UK Stanley and Karen Pigman COE with the 2024 Outstanding PhD Student Award. His research interests include wireless charging of electric vehicles, electric motors, and renewable energy integration.



Somasundaram Essakiappan (Senior Member, IEEE) received the B.E. degree in Electrical and Electronics Engineering from the College of Engineering Guindy, in 2007, and the M.S. and Ph.D. degrees in Electrical Engineering from Texas A&M University, in 2010 and 2014, respectively. He has been a Lead Electrical Engineer for Advanced Technologies at Trane Technologies since 2024, and an Adjunct Professor with the Department of Electrical and Computer Engineering, The University of North Carolina at Charlotte, since 2015. Previously, he was an R&D Engineering Manager with QM Power Inc., responsible for leading programs on new motor architectures and motor drives, from 2021 to 2023. Prior to that, he was a Teaching Professor and the Manager of the Flexible Energy Laboratories, Energy Production and Infrastructure Center, The University of North Carolina at Charlotte, from 2016 to 2021, where he developed and managed a high-power research and industrial testing laboratory for power electronic systems. He has published more than 50 research articles in various disciplines of power engineering and is an inventor of two U.S. patents and multiple pending patent applications. His research interests include power electronics for distributed energy integration, power quality and resiliency, and motors and drives. He is an active volunteer in professional societies and serves as a member of the Power Electronics Society Magazine Advisory Board and a reviewer for major journals and conferences. In the past, he has served as the Chair of the Young Professionals of IEEE Power Electronics Society, the Technical Program Chair for the 9th and 12th editions of the International Symposium on Power Electronics for Distributed Generation Systems (IEEE-PEDG), and the Publications Chair for the 10th and 11th Workshops on Wide Bandgap Power Devices and Applications (IEEE-WIPDA).



Madhav D. Manjrekar (Senior Member, IEEE) was born in 1972. He received the B.E. degree from the Government College of Engineering, University of Pune, India, in 1993, the M.Tech. degree from the Center for Electronic Design and Technology, Indian Institute of Science, India, in 1995, the M.S. degree from Montana State University, Bozeman, in 1997, the Ph.D. degree in electrical engineering from the University of Wisconsin, Madison, in 1999, and joined the University of North Carolina – Charlotte as an Associate Professor of Electrical & Computer Engineering in 2012. Prior to joining academia, he worked as the Vice President of Global Research and Innovation at Vestas, and previously has held various leadership and management positions at Siemens, Eaton and ABB. Dr. Manjrekar holds over 10 US and international patents, has published over 125 journal and conference papers, and has received multiple IEEE prize paper awards. He has advised over 30 PhD and MS students and currently serves as an Assistant Director and Chief Research Officer of the Energy Production and Infrastructure Center (EPIC) at the university.



Dan M. Ionel (Fellow, IEEE) received both the M.Eng. and Ph.D. degrees in electrical engineering from the Polytechnic University of Bucharest, Bucharest, Romania. His doctoral degree included a Leverhulme Visiting Fellowship with the University of Bath, Bath, U.K. He was a Postdoctoral Researcher with the SPEED Laboratory, University of Glasgow, Glasgow, U.K.

Previously to 2015, he worked in industry, most recently as Chief Engineer with Regal Beloit Corporation, Grafton, WI, USA, and before that as

Chief Scientist with Vestas Wind Turbines. He was also a Visiting Professor and a Research Professor with the University of Wisconsin and Marquette University, Milwaukee, WI, USA. He is currently Professor and the L. Stanley Pigman Chair in Power with the University of Kentucky, Lexington, KY, USA, where he is also the Director of the Power and Energy Institute of Kentucky and of the SPARK Laboratory. During his 2024 sabbatical in England, U.K., he was a Leverhulme Visiting Professor with University of Bath, expanding also the collaboration with University of Oxford, and was appointed as Honorary Professor at University College London (UCL).

Dr. Ionel has contributed to technological developments with long-lasting industrial impact, designed electric machines and drives with ratings between 0.002 and 10,000hp. He holds more than 40 patents, and has authored or coauthored two books, and more than 300 technical papers, including IEEE award winners. He served as Chair of large committees and conferences for the IEEE power societies. He was Editor of the IEEE Transactions on Sustainable Energy, and Editor-in-Chief of the Electric Power Components and Systems Journal. Dr. Ionel received the Cyril G. Veinott Award, the highest recognition for electromechanical energy conversion contributions from the IEEE Power and Energy Society.